

Issues in the inverse modeling of a single ring infiltration experiment

Michal Kuraz^a, Lukas Jacka^a, Johanna Ruth Bloecher^a, Matej Leps^b

^aCzech University of Life Sciences Prague, Faculty of Environmental Sciences, Department of Water Resources and Environmental Modeling

^bCzech Technical University in Prague, Faculty of Civil Engineering, Department of Mechanics

Abstract

This contribution addresses issues in the identification of soil hydraulic properties (SHP) of the top soil layer obtained from inverse modeling of a single ring (SR) infiltration experiment. The SR experimental data were obtained from a series of in situ experiments conducted on a highly heterogeneous mountainous podzolic soil profile. The SHP of the topsoil layer are very difficult to measure directly, since the thickness of the top soil layer is often much smaller than the depth required to embed the SR or Guelph permeameter device or to obtain undisturbed samples for further laboratory experiments.

A common problem with automatic optimization procedures are convergence issues. This problem is not trivial and can be difficult to deal with. We present a methodology to avoid convergence issues with the nonlinear operator. With this methodology, we can answer (1) to what extent the well-known SR experiment is robust enough to provide a unique estimate of SHP parameters using the unsteady part of the infiltration experiment and (2) whether all parameters are vulnerable to non-uniqueness. We validated our methodology with synthetic infiltration benchmark problems for clay and sand. To evaluate non-uniqueness, local optima were identified and mapped using a modified genetic algorithm with niching, which is not possible with commonly used gradient methods.

Our results show the existence of multimodality in, both, the benchmark problems and the real-world problem. This is an important finding as local optima can be identified, which are not necessarily physical and also for systems that do not exhibit multimodal grain size distributions. The identified local optima were distinct and showed different retention and hydraulic conductivity curves. The most physical set of SHP, could be identified with the knowledge of saturated water content, which makes it yet more obvious that expert knowledge is key in inverse modeling.

Keywords: soil hydraulic properties, inverse modeling of the Richards equation, FEM approximation of the Richards equation, differential evolution, application of dd-adaptivity algorithm, computational hydrology, computational soil science

1. Introduction

Soil hydraulic properties (hereafter SHP) are important for many hydrological models and engineer-

ing applications. The mountainous podzolic soil evaluated here is typical for the source areas of many major rivers in the Central European region. The top

layer of the soil plays a key role in the rainfall-runoff process, because it is the top-soil that separates the rainfall into surface runoff and subsurface runoff.

Due to the rocks present and the dense root system of the covering vegetation, and due to the possible extension of the representative elementary volume, it is often impossible to collect undisturbed samples of top-soil for laboratory measurements in order to obtain the SHP parameters (Jačka et al., 2014). The SHP of the topsoil are therefore very difficult to measure directly (Fodor et al., 2011; Jačka et al., 2014).

In our study, the well-known single ring (hereafter SR) method was used to obtain experimental input data (cumulative infiltration) for inverse modeling. The SR infiltrometer is a widely accepted, simple, robust field method, which is able to measure infiltration process, which affects the entire soil profile including the top-soil, and can sample a relatively large volume (depending on the diameter of the ring) (Cheng et al., 2011; Reynolds, 2008a). The SR infiltration experiment is an in situ experiment, which does not require soil samples to be collected, so the porous medium is kept relatively undisturbed. With the widely-used ring diameter of 30 cm, the affected porous media is far more representative than any soil sample we were able to collect. The top-soil can also be measured (with some alteration of the surface) using other well-known field infiltration methods, e.g. the tension infiltrometer or the well permeameter (Angulo-Jaramillo et al., 2000; Reynolds, 2008b).

The Richards equation (Richards, 1931) describes flow in variably saturated porous media. In order to model environmental processes and engineering applications with the Richards equation knowledge of

the SHP is essential. SHP can be summarized by the soil water retention curve and soil hydraulic conductivity curve. In this contribution, the SHP are parametrized with the frequently used Mualem-van Genuchten model (van Genuchten, 1980). We refer to this model as REVG.

Several studies compared REVG inverse modeling of tension infiltrometers (Simunek et al., 1998, 1999; Schwartz and Evett, 2002; Ventrella et al., 2005; Ramos et al., 2006; Verbist et al., 2009; Rezaei et al., 2016). They state that the retention curves obtained from inverse modeling using tension infiltrometer data are often not in good agreement with laboratory experiments on undisturbed samples. In particular, the saturated water content obtained from an inverse model of REVG is typically distinctly lower than the experimentally established value (Simunek et al., 1998; Verbist et al., 2009). There are various theories explaining the issue to be due to (i) the effect of hysteresis as the drying process in the laboratory differs from the wetting process in the field, (ii) the effect of entrapped air in the field (Fodor et al., 2011), where the saturation may not fully correspond to the pressure head, and (iii) the effect of macropores, which are excluded when a tension infiltrometer is used. Most importantly the soil samples usually examined in the laboratory are typically much smaller than the representative elementary volume (Scharnagl et al., 2011). However, several studies reported a close correspondence between the retention curve parameters obtained from laboratory experiments and from REVG analyses (Ramos et al., 2006; Schwartz and Evett, 2002). The identification of SHP from transient infiltration experiments has been a subject of numer-

ous publications in past decades (Inoue et al., 2000; Lassabatère et al., 2006; Kohne et al., 2006; Xu et al., 2012; Bagarello et al., 2017; Younes et al., 2017). Inoue et al. (2000) reported a close correspondence between the SHP obtained from the inverse modeling of dynamic transient infiltration experiments with those obtained from steady-state laboratory experiments, where the uniqueness of the inverse model was preserved by considering the dynamically changing pressure head, water content and even tracer concentration.

The non-uniqueness of the REVG inverse model is already a very well-known issue, and has been described by a number of publications over the last decades (Kool et al., 1985; Mous, 1993; Hwang and Powers, 2003; Binley and Beven, 2003; Kowalsky et al., 2004; Nakhaei and Amiri, 2015; Kamali and Zand-Parsa, 2016; Peña-Sancho et al., 2017). Mous (1993) defined criteria for model identifiability based on the sensitivity matrix rank, however numerical computation of the sensitivity matrix, which is defined by the derivatives of the objective function, often involves difficulties in managing truncation and round-off errors. Binley and Beven (2003) demonstrated on a real world case study of Sherwood Sandstone Aquifer that many different SHP parameters of macroscopic media can represent the layered unsaturated zone and provide acceptable simulations of the observed aquifer recharges. Mous (1993) explained that in case of the absence of water content data, the residual water content should be excluded from the identification to avoid non-uniqueness. However, Binley and Beven (2003) used a non-unique definition where both the unknown residual and saturated water

content were considered. The definition of a unique inverse function for identification of macroscopic media was treated in (Zou et al., 2001), where the recommended approach was to assemble the objective function from transient data of the capillary pressure and from the steady state water content data.

Another challenging issue is the treatment of the nonlinear operator of the Richards equation. Binley and Beven (2003) reported that 56% of the simulations were rejected during Monte Carlo simulations on a wide range of parameters, because of convergence problems. Their study did not mention explicitly why. We assume that these convergence issues originated from the nonlinear operator treatment – the outer iterations. It could be concluded, that if we use a simple Picard method for the nonlinear operator, and we increase the iteration criterion (which is typically referred to as h or θ tolerance), we will obtain a less accurate solution but we will also need less iterations for the Picard method. If we increase the criterion enough, we end up with a semi-implicit solution, where the constitutive functions in the Richards equation are evaluated from the previous time level solution – thus we just need a single outer iteration.

The following questions arise:

- Is it possible to approximate the unsteady SR experiment using the REVG model, where the only unknown parameters represent the thin topsoil layer, by a unique set of parameters?
- If not, are all parameters vulnerable to non-uniqueness?
- Are the parameters identified by inverse analysis of SR infiltration dependent on the treatment of

the nonlinear operator of the Richards equation?
Is there any benefit in using the accurate Newton or Picard iteration method, which can often lead to slow convergence or even divergence, or can we obtain a reasonable estimate with just the semi-implicit scheme (=evaluating nonlinear functions in the Richards equation from previous time level solution)?

The aim of this paper is to answer these questions. We approach these issues using a real-world problem aiming to identify SHP for the top soil layer in the experimental catchment Modrava in the Šumava National Park, Czech Republic. The SHP for lower soil layers were already identified through various field and laboratory experiments and by data processing

1.1. Comment on system of units applied in this manuscript

Due to spatial and temporal scales of all model scenarios evaluated in this manuscript, we preferred to make use instead of the base SI units the *non-SI units accepted for use with the SI*. The length [L] will be always given in [cm], and the time [T] will be always given in [hrs].

2. Methodology

This section is divided into two parts. The first part, section 2.1, is focused on assembling the experimental data, which were later used as input for the inverse model. The site description, the reconstruction of the parameters of the SHP for the lower profiles, and the processing of the experimental data is given.

The second part of the methodology covers issues in the REVG inverse model. Section 2.2 derives governing

equations and is given together with notes on the numerical stability of the REVG model for rotational symmetric problems. Section 2.3 discusses issues in creating the domain scheme and selecting appropriate boundary conditions, since it is not always easy to find an agreement between the mathematical model setup and physical interpretation. Section 2.4.1 concludes with a description of the construction of the objective function, and the methodology of the automatic calibration.

2.1. Obtaining the input data for the inverse problem

2.1.1. Site description and assembling the experimental data

The study site is located in the Šumava National Park, and has been described in (Jačka et al., 2014). The location of the site in a map of Modrava 2 catchment is presented by Jačka et al. (2012). A haplic podzol with distinct soil horizons is dominant on this site. The mean depths of the podzolic horizons are as follows:

- organic horizon O and humus horizon Ah altogether (the top-soil) 7.5 cm,
- eluvial bleached horizon E 12.5 cm,
- spodic horizons Bh_s and Bs 40 cm,
- weathered bedrock C.

The average groundwater table level can be roughly estimated at -280 cm below the surface.

The soil characteristics of the horizons below the top-soil are given in the table 1.

2.1.2. Obtaining SHP parameters for lower horizons

Guelph permeameter measurements (GP) were used to estimate the saturated hydraulic conductivity

Table 1: Fractions of the fine soil (< 2 mm) and skeleton (> 2 mm) and bulk density of the E and Bhs+Bs horizons.

horizon	clay < 2 μm	silt 2 μm – 0.05 mm	sand 0.05 – 2 mm	gravel > 2 mm	bulk density g.cm ⁻³
E	1%	20%	79%	32%	1.4
Bhs + Bs	7%	32%	61%	30%	1.3

of the lower horizons. The constant head GP method applied here is described in (Jačka et al., 2014). It is well known that pedotransfer functions work well for spodic and eluvial horizons characterized by high percentage of sand, without a distinct structure, and with a bulk density and porosity corresponding to a standard mineral soil. Parameters representing the retention curves for spodic horizons and eluvial horizon below the top-soil were estimated using the soil texture and the bulk density information with pedotransfer function implemented in Rosetta code (Schaap et al., 2001).

The estimated SHP for the lower horizons below the top soil are depicted in table 2.

2.1.3. Obtaining unsteady infiltration data for the top soil

The purpose of this section is to explain the methodology used for obtaining the data for the proposed inverse analysis.

For the O+Ah horizon smoothed experimental data from unsteady single ring (SR) infiltration were used as input for inverse modeling of REVG. The experimental setup was as follows. A steel ring 30 cm in inner diameter, 25 cm in length, and 2 mm in thickness was inserted into the soil to a depth of 12.5 cm,

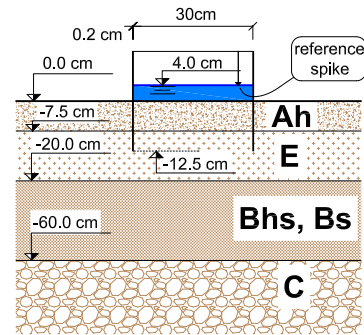


Figure 1: Scheme of the single ring infiltration experiment and the soil layers.

see figure 1. The depth of ponding was kept approximately at a constant level defined by a reference spike, which was placed 4 cm above the surface of the soil. The average experiment duration was 60 minutes.

A total of 22 SR experiments were conducted on the site. The experiments were evaluated as follows. In order to eliminate noise from the experimental values, each SR experiment data set was smoothed. It was observed that the Swartzendruber analytical model (Swartzendruber, 1987) of one-dimensional infiltration exhibited an excellent fitting quality, with a mean Nash-Sutcliffe model efficiency coefficient 0.9974. Thus we made use of exponential data smoothing. The Swartzendruber equation for cumulative infiltra-

Table 2: Soil hydraulic parameters for the lower horizons.

horizon	GP sites	experiment	θ_s [-]	α [cm ⁻¹]	n [-]	K_s [cm.hrs ⁻¹]	S_s [cm ⁻¹]
E	28		0.46	0.046	1.741	1.584	0
Bhs + Bs	19		0.47	0.022	1.450	0.540	0
C	8		0.50	0.035	4.03	3.060	0

tion states that

law (Buckingham, 1907)

$$I(t) = \frac{c_0 (1 - \exp(-c_1 \sqrt{t}))}{c_1} + c_2 t, \quad (1) \quad \mathbf{q} = -\mathbf{K}(\theta) \nabla H, \quad (2)$$

where I is the cumulative infiltration [L], and $c_{0,1,2}$ are parameters. The Swartzendruber model can estimate 1D saturated conductivity and sorptivity of the soil. However, the model does not account for water moving horizontally and therefore overestimates the hydraulic conductivity and gives no information on water retention or unsaturated hydraulic conductivity.

The Swartzendruber model was only considered as an exponential smoothing and interpolating function.

A statistical description of the Swartzendruber parameters and their fitting quality is given in (Jačka et al., 2016), see datasets collected on site 3. Representative mean values are as follows: $c_0 = 5.130 \text{ cm.hrs}^{-0.5}$, $c_1 = 1.13 \times 10^{-1} \text{ [-]}$, and $c_2 = 1.858 \text{ cm.hrs}^{-1}$. The parameter set was used to compute the infiltration curve with Eq. 1 for the identification of the SHP in the top soil layer.

2.2. Mathematical model of the field infiltration experiment – governing equation

The field infiltration experiment is characterized by variably saturated conditions ranging between unsaturated and saturated states. It is well known that the flux in porous media under variably saturated conditions can be expressed by the Darcy-Buckingham

where \mathbf{q} is the volumetric flux [L.T⁻¹], H is the total hydraulic head [L] defined as $H = h + z$, where h is the pressure head [L], z is the potential head [L], θ is the water content [-], and $\mathbf{K}(\theta)$ is the unsaturated hydraulic conductivity [L.T⁻¹]; in general it is a second order tensor. The relation $\theta(h)$ is referred to as the retention curve (van Genuchten, 1980).

The geometry of the flow is inherently three-dimensional, but the domain dimension can be reduced by considering the axisymmetric geometry. The law of mass conservation for incompressible flow in cylindric coordinates is expressed as (Bear, 1979).

$$-\frac{\partial V}{\partial t} = \frac{\partial q_r}{\partial r} + \frac{q_r}{r} + \frac{\partial q_\alpha}{\partial \alpha} + \frac{\partial q_z}{\partial z}, \quad (3)$$

where V is the volume function [-], r is the radial coordinate, α is the angular coordinate, z is the vertical coordinate, and $q_{r,\alpha,z}$ is the volume flux [L.T⁻¹]. The ring infiltration experiment is characterized by rotational symmetric flow, so the angular derivative vanishes. Then the governing equation for variably saturated and rotational symmetric flow is obtained by substituting the flux in (3) by the Darcy-Buckingham law (2). Together with the consideration of linear elasticity for a porous medium the variably saturated ax-

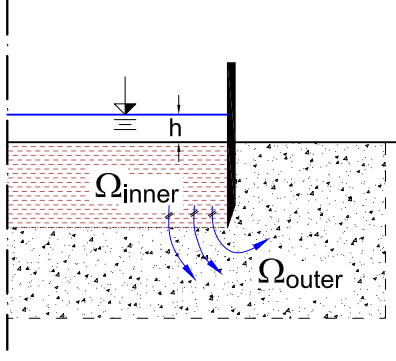


Figure 2: Scheme of the flow domain and the streamlines of infiltration experiment.

isymmetric flow in isotropic media is governed by

$$\left(\frac{d\theta}{dh} + S_s \frac{\theta(h)}{\theta_s} \right) \frac{\partial h}{\partial t} = \frac{\partial K(h)}{\partial z} \frac{\partial H}{\partial z} + \frac{\partial K(h)}{\partial r} \frac{\partial H}{\partial r} + c(\mathbf{x}) \frac{\partial H}{\partial r}, \quad (4)$$

where S_s is the specific storage [L^{-1}], θ_s is the saturated water content [-], $c(\mathbf{x})$ is the coefficient of the convection for r coordinate [T^{-1}], which is explained below, and the vector x is a vector of the spatial coordinates $\mathbf{x} = \begin{pmatrix} r \\ z \end{pmatrix}$.

Let us consider the model of the infiltration experiment depicted in figure 2. Let the entire flow domain $\Omega = \Omega_{inner} \cup \Omega_{outer}$, where Ω_{outer} is the flow domain outside the infiltration ring and Ω_{inner} is the flow domain within the infiltration ring, exactly as depicted in figure 3. It is apparent that the streamlines inside subdomain Ω_{inner} are parallel, but the streamlines outside the infiltration ring (inside Ω_{outer}) are only axisymmetric. The convection coefficient $c(\mathbf{x})$ is then defined as follows

$$c(\mathbf{x}) = \begin{cases} 0, & \forall \mathbf{x} \in \Omega_{inner} \\ \frac{1}{r} K(h), & \forall \mathbf{x} \in \Omega_{outer}. \end{cases} \quad (5)$$

Note that we should avoid using the coordinates, where $r = 0$.

2.3. Domain scheme, initial conditions and boundary conditions

The goal of the model was to achieve cumulative infiltration – the cumulative flux over the top Dirichlet boundary. The computational domain is depicted in figure 3 together with the discretization mesh. The location of the top boundary was natural – the soil surface. Inside the ring, a Dirichlet condition defines the ponding depth; outside the infiltration ring a Neumann condition defines the no-flow boundary. Locating the bottom boundary was more problematic. The following options are available

- the no-flow boundary (Neumann)
- the free drainage boundary (Neumann)
- the groundwater level - zero pressure head (Dirichlet)

It is apparent that the wetting front originating from our infiltration experiment affects the soil column only to a certain depth. Defining the Neumann no-flow boundary at a sufficient depth would therefore probably not have a significant effect on the derivative of the solution of (4) at the top boundary. At the same time, the only physically acceptable location of the no-flow boundary is the groundwater table. The second option – the free drainage boundary – would be completely incorrect for any depth. The free drainage boundary defines fluxes that probably do not appear in our system at all. Above all, if we consider here the initial condition as a hydrostatic state, and so

$$\frac{\partial h}{\partial z}(x) = -1, \quad \forall x \in \Omega. \quad (6)$$

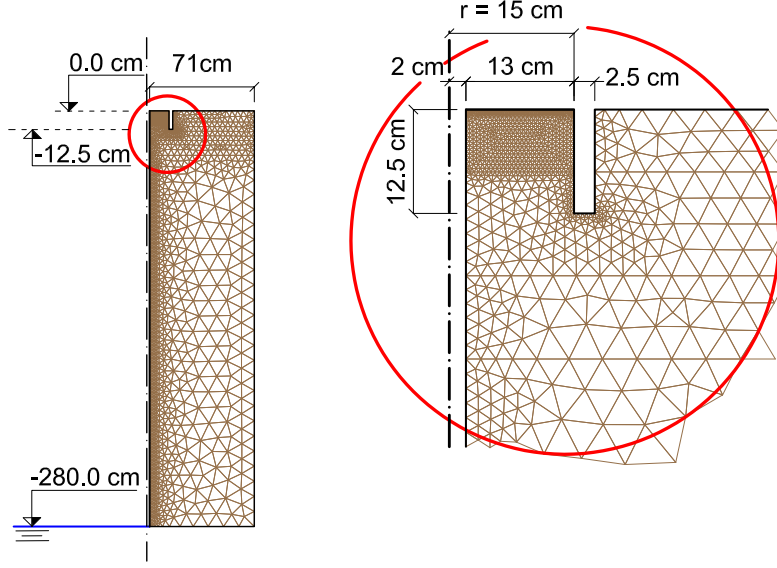


Figure 3: Scheme of the computational domain geometry and domain triangularization.

The free drainage boundary condition, which is defined as

$$\frac{\partial h}{\partial \mathbf{n}}(x) = 0, \quad \forall (x, t) \in \Gamma_{\text{free drainage}} \times [0, T]. \quad (7)$$

is in a conflict with the initial condition (since the outer normal vector $\mathbf{n} = \begin{pmatrix} 0 \\ -1 \end{pmatrix}$), which is again physically incorrect, and produces extra computational costs. The computational process, that is produced at the bottom boundary in the beginning of the simulation with such boundary setup, originates from the initial and boundary condition mismatch, and has no physical meaning.

It turns out that the only physically correct boundary condition for the bottom boundary is either the Neumann no-flow boundary or Dirichlet boundary both at the groundwater table. The average depth of the groundwater table was known, it is approximately -280 cm below the surface. With this particular setup the domain became extremely narrow and deep, see figure 4.

2.3.1. Stability restrictions of convection dominant problems

The equation (5) refers to coefficient of the first order derivative term in (4), and so the well known stability restrictions for the numerical solutions of the convection-diffusion problems appear here Christie et al. (1976). The Peclet number representing the numerical stability of convection-diffusion problems is defined as (Knobloch, 2008)

$$Pe = \frac{c\Delta x}{2D}, \quad (8)$$

where c is the convection coefficient defined in (5), Δx is the discretization step, and D is the diffusion (for isotropic setup). Based on the definitions given above, equation (8) can be formulated as

$$Pe = \frac{\frac{1}{r}K(h)\Delta x}{2K(h)} = \frac{\Delta x}{2r}. \quad (9)$$

Since our mesh is triangular, Δx can be roughly assumed to be the greatest triangle altitude (since we

assume some mesh quality properties). Then a sufficient distance from the axis of anisotropy is such that the Peclet number is sufficiently low. If we want to make our computation free of the well known spurious oscillations Christie et al. (1976); Roos et al. (1996), a sufficiently low Peclet number $Pe \leq 1$ is required. Therefore, the distance from the axis of anisotropy is given by the domain discretization step at the left hand side boundary. The selected discretization step at the left hand side boundary was assumed as $\Delta x = 2$ cm. The domain was therefore detached by 2 cm from the axis of anisotropy, and thus the Peclet number was 0.5 only.

2.3.2. Domain shape restrictions

Since Dusek et al. (2009) mentioned several difficulties with incorrect triangular mesh setup while modeling the SR experiment, we tried to avoid possible numerical issues connected with domains with sharp spikes.

It is well known, that sudden changes in domain shapes, spikes and discontinuities yield numerical difficulties (e.g. the Lipschitz boundary restrictions (Braess, 1997)). In order to avoid computational difficulties during the automatic calibration procedure the infiltration ring thickness was oversized to 2.5 cm. It is obvious that the real ring thickness is much smaller (in our case 2 mm), but using the real ring thickness yields possible numerical issues. It is expected, that oversizing the ring thickness does not significantly affect the fluxes through the top Dirichlet boundary, which is the only important part of the solution of (4) for our calibration process.

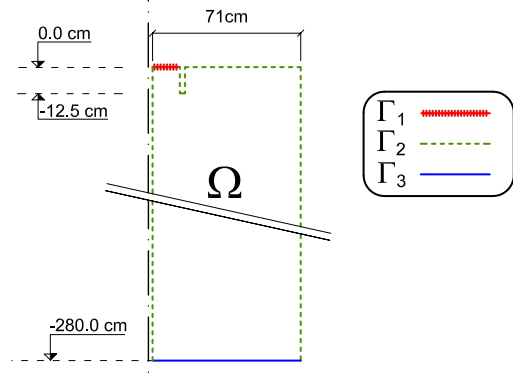


Figure 4: Scheme of the computational domain geometry and the domain boundaries.

2.3.3. Initial and boundary condition setup

As discussed in 2.3.1 the left hand side boundary was located at $r = 2$ cm. The right hand side boundary was located at a distance $r = 73$ cm, it means 60 cm from the infiltration ring.

The locations of the domain boundaries are depicted in figure 4. The boundary conditions are specified as follows (with the reference level $z = 0$ located at the top boundary)

$$\begin{aligned} h(x, t) = 4 \text{ cm} &\Rightarrow H(x, t) = 4 \text{ cm}; \quad \forall (x, t) \in \Gamma_1 \times [0, T], \\ \frac{\partial H}{\partial \mathbf{n}} &= 0; \quad \forall (x, t) \in \Gamma_2 \times [0, T], \\ h(x, t) = 0 \text{ cm} &\Rightarrow H(x, t) = -280.0 \text{ cm}; \quad \forall (x, t) \in \Gamma_3 \times [0, T]. \end{aligned} \quad (10)$$

where T is the simulation end time [T], and \mathbf{n} is the boundary normal vector.

The initial condition was assumed as a steady state solution of (4) with the boundary $\Gamma_1 \cup \Gamma_2$ assumed as a no-flow boundary – thus the entire domain Ω was considered to be in hydrostatic state. The initial condition states that

$$H(x) = -280.0 \text{ cm}; \quad \forall x \in \Omega, \quad (11)$$

and thus $\frac{\partial h}{\partial z} = -1$.

2.3.4. Numerical solution, temporal and spatial discretization, automatic calibration methodology

Equation (4) was implemented into the DRUtes library (Kuraz and Mayer, 2008). It is an object-oriented library written in Fortran 2003/2008 standard for solving nonlinear coupled convection-diffusion-reaction type problems. The problem was approximated by the linear finite element method for spatial derivatives and Rothe's method for temporal derivatives. The nonlinear operator was treated with the Schwarz-Picard method – an adaptive domain decomposition (*dd*-adaptivity) – with the ability to activate and deactivate subregions of the computational domain sequentially (Kuraz et al., 2013a, 2014, 2015).

The domain was non-uniformly discretized by a triangular mesh. The smallest spatial step was considered for the top layers inside the infiltration ring, close to the Dirichlet boundary. The mesh is depicted on figure 3. The minimum spatial length was 0.5 cm, and the maximum spatial length was 20 cm. The domain was discretized with 2097 nodes and 3861 elements. The coarse mesh for the *dd*-adaptivity method was a uniform quadrilateral mesh with elements 17.75×28.0 cm, i.e. a total of 40 coarse elements and 55 nodes. The purpose of the coarse mesh is to organize the elements of the domain triangulation into so-called clusters, which form a basic unit for the adaptive domain decomposition used here for solving the nonlinear problem, details can be found in (Kuraz et al., 2015).

The spatial and temporal discretization of (4) leads to sequential solutions of systems of non-linear equations, see e.g. (Kuraz et al., 2013a). The system was

linearized as discussed in Kuraz and Mayer (2013); Kuraz et al. (2013b), and so the numerical solution requires an iterative solution of

$$\mathbf{A}(\mathbf{x}_l^k)\mathbf{x}_l^{k+1} = \mathbf{b}(\mathbf{x}_l^k), \quad (12)$$

where k denotes the iteration level, and l denotes the time level, until

$$\|\mathbf{x}_l^{k+1} - \mathbf{x}_l^k\|_2 < \varepsilon, \quad (13)$$

where ε is the desired iteration criterion. The iterations required for (12) to converge are denoted as the outer iterations. It is apparent that the number of required outer iterations depends on the ε criterion.

The method (12) degenerates into a kind of semiexplicit approximation if the error criterion ε was "infinitely huge" – it means taken from the extended real numbers, $\varepsilon \in \overline{\mathbb{R}}$, and assigned as $\varepsilon = +\infty$. This semiexplicit approximation is denoted as

$$\mathbf{A}(\mathbf{x}_{l-1})\mathbf{x}_l = \mathbf{b}(\mathbf{x}_{l-1}). \quad (14)$$

This semiexplicit method always requires just a single outer iteration. With a short time step the method converges to the exact solution. For inappropriate time steps, the method diverges from the exact solution faster than the method (12). Nonetheless, the method (14) is free of possible issues related to the convergence of the nonlinear operator.

The infiltration flux is obtained from the numerical derivative of the solution of (4), and it is well known that inaccurate approximation of the capacity term (time derivative term) yields inaccurate mass properties (Celia et al., 1990). We are aware of the

possible impact of spatial and temporal discretization on the identified SHP values. We are also aware of possible difficulties with convergence of the linearized discrete system (12) for certain combinations of SHP parameters during the automatic calibration, as discussed by Binley and Beven (2003).

Following the concerns about effects of numerical treatment for the identified values of SHPs parameters a specific automatic calibration methodology was proposed. The technique is explained in brief in figure 5, and details are given in the following paragraph.

- (i) Proceed the calibration procedure with the quasi-explicit stable numerical technique for treating the nonlinear operator explained in equation (14), with the initial time step $t_{init} = 10^{-6}$ hrs (note that all real numbers are represented with double precision in our implementations), and for each subsequent time level l , $\Delta t_l = 1.05\Delta t_{l-1}$, where $l = \{1, n_t\}$, where n_t is the number of time levels used for the temporal discretization. The ranges of parameters for this calibration are given in table 3, so the maximal values of SHP are defined as a vector $\mathbf{p}_{r_f, max}$, and the minimal values are defined as a vector $\mathbf{p}_{r_f, min}$. So initially the ranges are extremely broad and exceeding even the physically acceptable values. The spatial discretization for this step of calibration was given in the beginning of this section – 2097 nodes and 3861 elements. Let us assume that this discretization is given by a mesh density function $\Delta(\mathbf{x})^{r_f}$. The function $\Delta(\mathbf{x})^{r_f}$ is understood as a spatial distribution of mesh size density, which was used as an input for the mesh generator T3D (Rypl, 2004). The superscript r_f

defines the refinement level, where $r_f = 0$ at this initial stage, and the vector \mathbf{x} refers to spatial coordinates inside the domain Ω .

- (ii) Let us presume that this inverse model will have more than just a single solution.

- Then this calibration will generate vectors of SHP values $\mathbf{p}_{r_f}^{i_e}$, where the superscript $i_e = \{1, ..., n_e\}$, where n_e denotes the number of local extremes.

- (iii) To validate the inverse modeling results, select physically acceptable local extremes with good fitting qualities, and create a scatter plot of the objective function in the local extreme neighborhood with improved temporal integration and spatial discretization. For each $\mathbf{p}_{r_f}^{i_e}$ from the acceptable solutions the neighborhood is defined as

$$\begin{aligned} \mathbf{p}_{r_f, max}^{i_e} &= 1.20\mathbf{p}^{i_e}, \\ \mathbf{p}_{r_f, min}^{i_e} &= 0.70\mathbf{p}^{i_e}. \end{aligned} \quad (15)$$

The improvement of the numerical treatment will be processed as follows:

Increase the discretization level

$$r_f = r_f + 1, \quad (16)$$

and update the following parameters of the numerical treatment

$$\begin{aligned} \Delta(\mathbf{x})^{r_f} &= \frac{\Delta(\mathbf{x})^{r_f-1}}{2}, \\ \varepsilon^{r_f} &= 10^{-3} \text{ cm} \quad \text{if } r_f = 1, \quad \text{else} \quad \varepsilon^{r_f} = \frac{\varepsilon^{r_f-1}}{10}, \\ t_{init}^{r_f} &= \frac{t_{init}^{r_f-1}}{10} \text{ hrs.} \end{aligned} \quad (17)$$

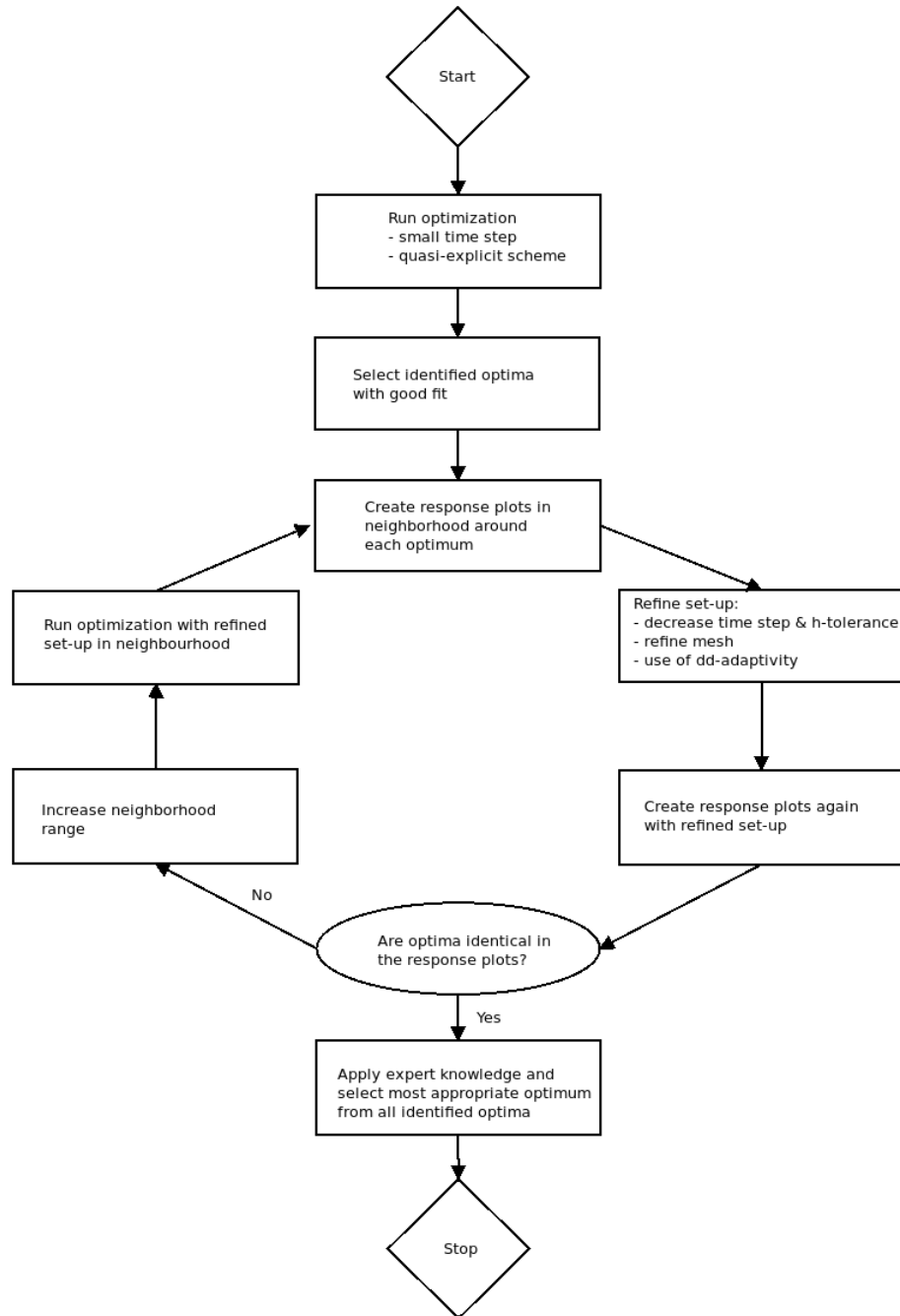


Figure 5: The proposed methodology for the automatic calibration avoiding effects of numerical treatment for the identified SHPs values.

If $r_f > 0$, then the nonlinear problem represented now by (12) will be solved by the Schwarz-Picard method – an adaptive domain decomposition (Kuraz et al., 2015). To validate the inverse model solution for $r_f - 1$ discretization level perform the following:

(a) Compare the scatter plots for the selected local extreme i_e created with discretization r_f and $r_f - 1$. For this local extreme a vector of SHP parameters $\mathbf{p}_{r_f-1}^{i_e}$ is handled.

(b) If the optima refer to significantly different SHP parameters.

- Proceed the calibration again with the new parameter range defined as $\mathbf{p}_{max} = 1.2\mathbf{p}_{r_f-1}^{i_e}$ and $\mathbf{p}_{min} = 0.8\mathbf{p}_{r_f-1}^{i_e}$. This new calibration will update the vector $\mathbf{p}_{r_f-1}^{i_e}$ to $\mathbf{p}_{r_f}^{i_e}$.
- Increase the discretization level r_f as $r_f = r_f + 1$, perform the update (17), return to (iii)a, and check the condition (iii)b.

(c) else

- Exit the calibration process.

The following sections will further explain the definition of the objective function and the parameter identification algorithm.

2.4. Optimization

2.4.1. Parameter identification, a definition of the objective function

The soil hydraulic parameters (SHP) of the top soil that will be identified were specified in section 2.1.2. Since the parameters will be identified us-

ing a stochastic method, we have to introduce a physically reasonable range for each parameter. The ranges for the SHP are specified in table 3.

The objective function is defined in the following paragraph.

Let $\bar{I}(\mathbf{p}, t)$ be the cumulative infiltration obtained from solving the mathematical model (4) bounded by the initial and boundary conditions defined in section 2.3 for a certain vector of SHPs parameters \mathbf{p} considered as

$$\bar{I}(\mathbf{p}, t) = \frac{\int_0^t \int_{\Gamma_1} -K \frac{\partial H}{\partial n}(t) d\Gamma_1 dt}{\int_{\Gamma_1} d\Gamma_1}. \quad (18)$$

Let $I(t)$ be the cumulative infiltration defined by (1) with parameters given in section 2.1.3. Then the objective function was defined for three different criteria in order to avoid ill-posed objective function definition.

The objective functions were defined as follows:

I. First criterion Ψ_1 was defined as L_2 norm of the difference between the experimental and model data and thus

$$\Psi_1(\mathbf{p}) = \sqrt{\int_0^{T_{end}} (\bar{I}(\mathbf{p}, t) - I(t))^2 dt}, \quad (19)$$

where T_{end} is the final simulation time $[T]$, which is indeed the root mean square error for continuous functions.

II. Second criterion was the L_∞ norm of the difference between the experimental and model data

Table 3: Ranges of SHPs (\mathbf{p}_{max} and \mathbf{p}_{min}) for identifying the SHPs in the top-soil layer for *refinement level* $r_f = 0$. Note that the initial ranges are extremely broad especially for the saturated water content θ_s . This broad range was selected in order to explore the uniqueness of the REVG inverse model of SR experiment even beyond the physically acceptable solutions.

θ_s [-]	α [cm ⁻¹]	n [-]	K_s [m.s ⁻¹]	S_s [m ⁻¹]
0.25 – 0.90	$1 \times 10^{-4} - 5.000 \times 10^{-2}$	1.05 – 4.5	0.300 – 300.0	0.0 – 0.1

and thus

$$\Psi_2(\mathbf{p}) = \sup \left(\sqrt{(\bar{I}(\mathbf{p}, t) - I(t))^2} \right), \quad t \in (0, T_{end}). \quad (20)$$

III. Third criterion was considered as the difference between the infiltration rates (final derivatives) between the model data and the experimental data

$$\Psi_3(\mathbf{p}) = \sqrt{\left(\frac{d\bar{I}(\mathbf{p}, T_{end})}{dt} - \frac{dI(T_{end})}{dt} \right)^2}. \quad (21)$$

We conducted multi-objective optimization. However, it is apparent that minimizing the objective function (19) also minimizes the objective functions (20) and (21). The aim of this multi-objective definition was to improve the conditioning of this inverse problem. If we only considered the objective function (19), then we were probably able to obtain the same solution as with this multi-objective definition with slower convergence of optimization procedure only (the selection of the optimization algorithm will be explained in the following section 2.4.2). This multi-objective function definition is based on our experience from previous attempts of inverse analysis of this infiltration problem.

2.4.2. Optimization algorithm

In this contribution we used the modified genetic algorithm GRADE (Ibrahimbegović et al., 2004; Kucerovala, 2007) supported by niching method CERAf (Hrstka and Kučerová, 2004) enhancing the algorithm with memory and restarts. GRADE is a real-coded genetic algorithm combining the ideas of genetic operators: cross-over, mutation and selection taken from the standard genetic algorithm and differential operators taken from differential evolution. When GRADE converges, the current position of the optimization algorithm is marked as a local extreme and a forbidden area is built around it in order to forbid the optimization algorithm to fall into the same local extreme again. The main setting of the optimization procedure was as follows: the population of the genetic algorithm contains 30 independent solutions, the whole identification stops after 20.000 objective function evaluations and a local extreme was marked after 600 evaluations without any improvement.

2.4.3. Multi-objective Optimization

In this contribution Average Ranking (AR) (Leps, 2007) was used to deal with multi-objective definition. It sums ranks of the objective functions instead of the objective functions' values. Therefore, no weights are needed, however, the Pareto-dominance is not preserved as described in Vittingerova (2010). An application of the AR algorithm to parameters identifica-

tion can be found in Kuráží et al. (2010).

2.5. Benchmark evaluations

The purpose of this section is to evaluate the robustness of the proposed methodology, and to experimentally validate the following research hypotheses, which has arisen in this manuscript.

1. The SHP properties can be identified from the cumulative volume fluxes measured at Dirichlet boundary.
2. Nevertheless, the estimated SHP properties are vulnerable for non-uniqueness.
3. The estimated SHP properties are affected by accuracy of the numerical solution of the Richards equation, however, the less accurate solution of the Richards equation can be used as an estimator of the inverse model solution.

For simplicity only a one-dimensional Richards equation problem was considered here. Dirichlet boundary conditions were presumed for both boundaries. The model setup state as follows. Computational domain was $\Omega = (0, 100 \text{ cm})$, and the boundary and initial conditions stated as follows

$$\begin{aligned} h(x, t) &= 0 \text{ cm}, \quad \forall (x, t) \in \Gamma_{bot} \times t \in [0, T_{end}) \\ h(x, t) &= 0 \text{ cm}, \quad \forall (x, t) \in \Gamma_{top} \times t \in [0, T_{end}) \\ H(x, t_0) &= 0 \text{ cm}, \quad \forall x \in \Omega, \end{aligned} \quad (22)$$

where $\Gamma_{bot} = 0.0 \text{ cm}$, $\Gamma_{top} = 100.0 \text{ cm}$, and $T_{end} = 10^{-1} \text{ hrs}$. Two distinguished soil types were considered here – clay loam and sand, the parameters were obtained from (van Genuchten et al., 2009), and are given in table 4

The computational domain Ω was uniformly discretized with $\Delta x = 0.5 \text{ cm}$, the initial time step was $\Delta t = 10^{-7} \text{ hrs}$, and the error criterion from (13) for solving the nonlinear system (12) was $\varepsilon = 10^{-3} \text{ cm}$.

The reference solutions both for sand and gravel media were obtained from cumulative flux over the top Dirichlet boundary Γ_{top} .

For the given reference solutions the inverse modeling algorithm described in section 2.4.2 was employed for searching the original SHP parameters in broad ranges given in table 3. In the first stage the numerical setup of the Richards equation solver was identical with the one used for the reference solution. In the second stage the accuracy of the numerical treatment of the Richards equation was sharply decreased. The spatial discretization became twice as much coarser with $\Delta x = 1.0 \text{ cm}$, and, more importantly, the nonlinear system (12) was treated with semiexplicit method (14), which applies for $\varepsilon \rightsquigarrow +\infty$.

And thus in total four inverse modeling experiments were conducted – two for clay medium and two for sand medium – the first set with the original numerical treatment and the second set with the coarser discretization setup.

Results of the benchmark problem are given in table 5. For all four benchmark problems the inverse modeling algorithm has found several local optima, and the low value of an objective function doesn't necessarily point to the correct solution. Thus the problem is multi-modal. Several distinct SHP parameter sets can lead to acceptable solutions. However, the most distinct SHP parameter is the saturated water content θ_s . It turns out that an expert knowledge is required here, to select an acceptable solution of this

Table 4: SHP properties for benchmark models.

	α [cm ⁻¹]	n [-]	θ_r [-]	θ_s [-]	K_s [cm.hrs ⁻¹]
clay loam	0.019	1.31	0.095	0.41	6.24
sand	0.145	2.68	0.045	0.43	29.7

Table 5: Results of the benchmark problem. The grey highlighted rows refer to the physically acceptable solution of this benchmark inverse problem, and the red highlighted rows contain the exact solution of this inverse problem.

		extreme	parameters				objective function (19)
			α [cm ⁻¹]	n [-]	θ_s [-]	K_s [cm.hrs ⁻¹]	Ψ_1
clay	exact solution		1.900×10^{-2}	1.31	0.41	6.24	
	1 st stage	1	2.037×10^{-2}	1.322	0.396	6.226	4.787×10^{-2}
		2	1.152×10^{-2}	1.05	0.2502	7.0108	2.830×10^{-1}
		3	1.280×10^{-4}	1.146	0.900	94.904	3.724×10^{-1}
	2 nd stage	1	1.994×10^{-2}	1.350	0.466	7.005	5.606×10^{-1}
		2	9.418×10^{-2}	3.799	0.250	3.863	1.290
		3	1.998×10^{-2}	1.350	0.266	6.992	6.542×10^{-1}
sand	exact solution		1.450×10^{-1}	2.68	0.43	29.7	
	1 st stage	1	3.941×10^{-2}	1.050	0.250	35.563	2.978×10^{-2}
		2	2.629×10^{-2}	1.087	0.587	37.877	2.406×10^{-2}
		3	1.540×10^{-1}	2.654	0.460	30.145	2.199×10^{-2}
	2 nd stage	1	4.247×10^{-2}	1.127	0.256	69.785	1.578×10^{-2}
		2	1.222×10^{-1}	2.455	0.35	32.633	1.400×10^{-2}

inverse problem.

In the second stage the inverse problem was solved with less accurate discretization technique. It is apparent, that even the less accurate (but oscillations free) semi-explicit method for treatment of the nonlinear Richards equation operator has given reasonable estimates of the SHP parameters.

tal 10.000 samples of the objective function (19) were evaluated, in order to obtain the Total Sobol Index for each parameter (Saltelli et al., 2000). The values of the Total Sobol Indices are given in table 6. Since the evaluated Total Sobol Index for each parameter was nearly 0.9, our model exhibits an excellent sensitivity for all SHPs parameters.

3. Results and discussion

The first procedure, which is typically required before proceeding the inverse modeling procedures, is the global sensitivity analyses on selected parameter ranges, see table 3. For simplicity the sensitivity analyses was conducted just for the first objective function (19). This strategy is in line with the statements given in the last paragraph of the section 2.4.1. In to-

Table 6: Total Sobol indices for the searched SHPs parameters.

parameter	α	n	K_s	θ_s	S_s
Total Sobol Index	0.850	0.921	0.876	0.868	0.884

The first run with discretization level $r_f = 0$ generated after 40.000 objective function calls (each call took approximately 3 min, executed on 32-core In-

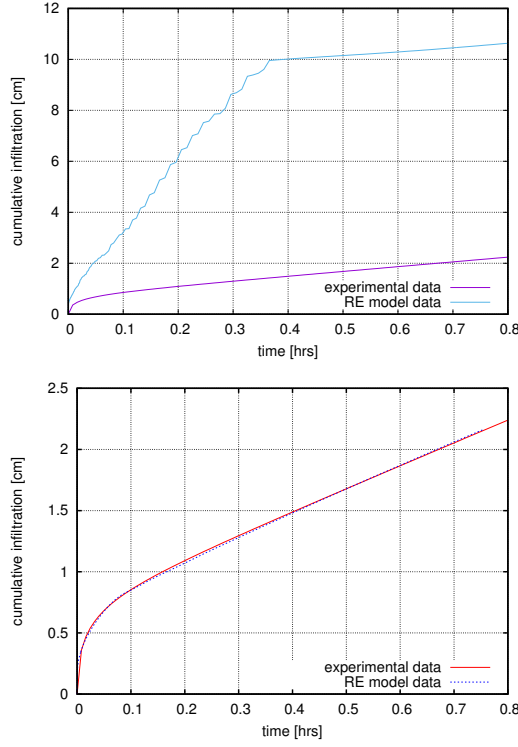


Figure 6: Left: Local extreme 2 – bad fitting properties, Right: Local extreme 5 – good fitting properties.

tel(R) Xeon(R) CPU E5-2630, bogomips 4801.67) the local extremes are given in table 7, where the gray lines refer to local extremes with bad fitting properties (extremes 1-5), the local extremes 6-8 refer to inverse model solutions with good fitting properties. The results were visually inspected. An example of bad fitting dataset is depicted on figure 6 - left, and the example of the good fitting dataset is depicted on figure 6 - right. Solution for each dataset is given in Appendix.

In the next step the refinement level was increased, new mesh was generated, the new mesh discretized the domain into 4503 nodes and 8488 elements. The Picard criterion for the pressure head was refined for 1×10^{-3} cm, and the initial time step was 1×10^{-7} hrs. Only the local extremes 6-8 from table 7 were further evaluated.

For the local extreme 6, the refined numerical treatment $r_f = 1$ has not affected the objective function, the figure 7 depicts two examples of the scatter plots – for the parameter α and n . The scatter plots of all parameters are given in Appendix. The response for the α parameter (figure 7 - left) seems adequate, which wasn't the case of n parameter (figure 7 - right). It turns out that for this parameter set the objective function exhibits poor local sensitivity. However, this wasn't the case of the other local extremes, see figure 8 - left.

The local extreme 8 is characterized by nonzero specific storage S_s . However, if we look closer to the scatter plot 8 - right, it becomes apparent, that the specific storage should vanish even for this parametric set. Both local extremes 7 and 8 exhibit similar local sensitivity and similar response for changing the r_f level, as the one depicted in figure 8 - right.

For the local extremes 7 and 8, the inverse process was restarted with discretization level $r_f = 1$. The new inverse solution was searched in vicinity of both extremes, and thus two different narrow parameter ranges were defined now – see table 8. Based on the results discussed above the specific storage was assumed to vanish from our model.

With the increased discretization level the runtime for each simulation increased for 20 minutes on hardware equipment specified above. But since the parameter range was already relatively narrow, the optimization algorithm converged fast and the solution was achieved after 1000 iterations. The process was executed in parallel on 16-core CPU architecture, and thus the results were obtained in less than one day.

The updated solutions maintained similar fitting

Table 7: Identified local extremes of Pareto front during the first run of parameter search procedure.

no.	α [cm ⁻¹]	n [-]	θ_s [-]	K_s [cm.hrs ⁻¹]	S_s [cm ⁻¹]
1	2.447×10^{-4}	2.45	0.25	2.500×10^{-2}	4.190×10^{-3}
2	1.010×10^{-3}	0.6517	0.271	1.092	2.879×10^{-2}
3	1.840×10^{-2}	2.098	0.353	1.092	1.845×10^{-4}
4	1.570×10^{-3}	1.968	0.720	2.070	1.053×10^{-5}
5	1.500×10^{-3}	1.586	0.720	1.093	7.641×10^{-3}
6	2.580×10^{-3}	2.152	0.401	1.095	0
7	3.802×10^{-3}	1.279	0.594	1.165	0
8	2.550×10^{-3}	1.384	0.254	1.119	1.922×10^{-4}

Table 8: Ranges of SHPs (\mathbf{p}_{max} and \mathbf{p}_{min}) for identifying the SHPs in the top-soil layer for refinement level $r_f = 1$.

extreme	θ_s [-]	α [cm ⁻¹]	n [-]	K_s [cm.hrs ⁻¹]
7	0.475 - 0.712	3.042×10^{-3} - 4.562×10^{-3}	1.023 - 1.534	0.932 - 1.398
8	0.203 - 0.305	2.040×10^{-3} - 3.060×10^{-3}	1.107 - 1.661	0.8952 - 1.342

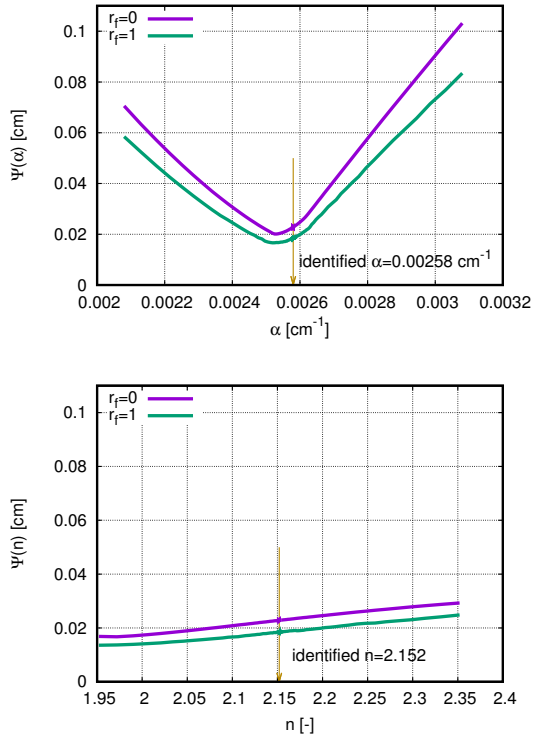


Figure 7: Scatter plots of the objective function (19) for the parameter α (left) and n (right) for extreme 6.

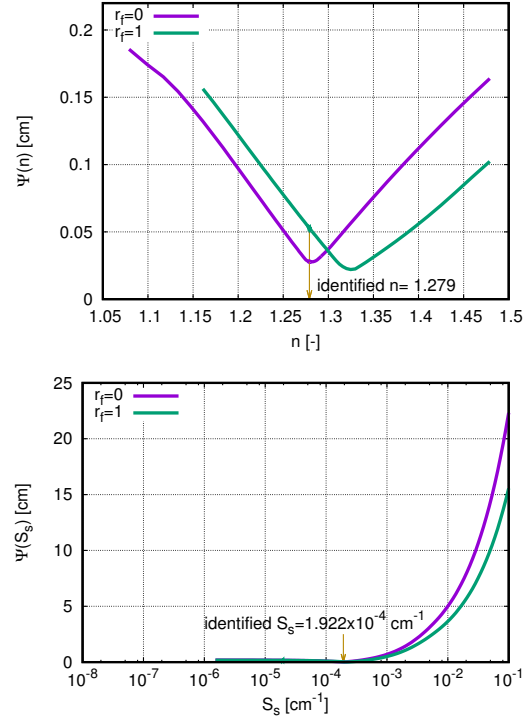


Figure 8: Scatter plots of the objective function (19) for the parameter n at extreme 7 (left) and S_s at extreme 8 (right)

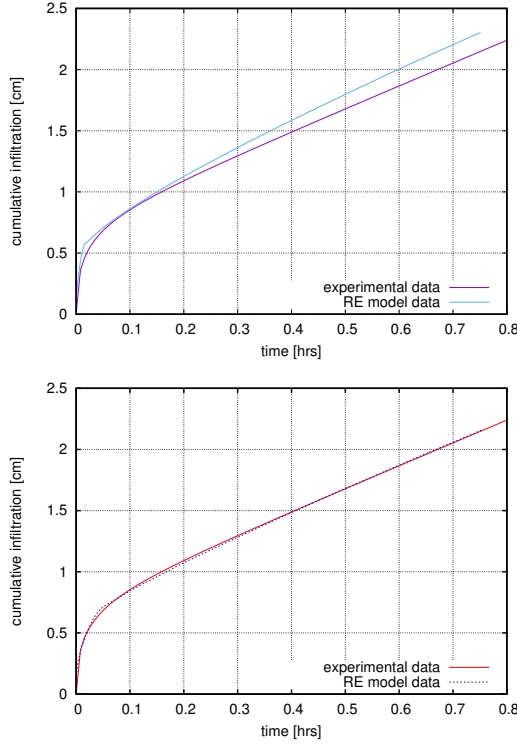


Figure 9: Left: Local extreme 7 infiltration curve for the original parameter set obtained at $r_f = 0$ and solved on model with discretization $r_f = 1$, right: solution for the updated parameter set in vicinity of the extreme 7.

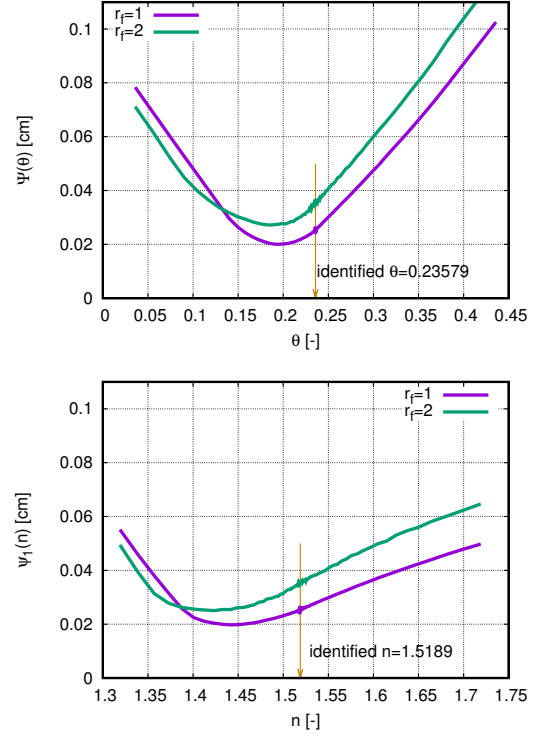


Figure 10: Scatter plots for $r_f = 1, 2$ for extreme 8 for parameters θ_s and n .

qualities as the solutions obtained at $r_f = 0$, see figure 9 - right. Whereas the solution depicted on figure 9 - left was created with SHPs dataset obtained at previous discretization level ($r_f = 0$) tested on model with increased discretization level ($r_f = 1$).

In order to evaluate the results obtained at $r_f = 1$ discretization level, the discretization level was increased again for $r_f = 2$. New mesh was generated with 6843 nodes and 13122 elements. Initial time step was now set for 1×10^{-8} hrs, and the Picard criterion was set for 1×10^{-4} hrs. New scatter plots were generated, an example is given in figure 3. For all scatter plots see Appendix.

The location of peaks of the scatter plots for these two sequential discretization levels don't vary significantly, and so no further refinements were required. The table 7 provides the final results of this inverse

problem. As mentioned above the solution for the extreme 6 didn't require further updates, except for the n parameter, which has been slightly updated from the identified value 2.152 for new value 1.950 in accordance with the scatter plot in figure 7 - right.

4. Conclusions

The purpose of this paper was to evaluate the capability of an unsteady part of the well known single ring infiltration experiment for estimating soil hydraulic properties, namely the water retention curve. The main research question was whether the cumulative infiltration curve representing the unsteady part of the single ring experiment is robust enough to give a unique definition for soil hydraulic properties, particularly van Genuchten's parameters α , and n , saturated water content θ_s , and obviously the saturated

Table 9: The resulting SHP data sets.

no.	α [cm ⁻¹]	n [-]	θ_s [-]	K_s [cm.hrs ⁻¹]	S_s [cm ⁻¹]
6	2.580×10^{-3}	1.950	0.401	1.095	0
7	3.229×10^{-3}	1.442	0.513	1.100	0
8	2.276×10^{-3}	1.519	0.236	1.036	0

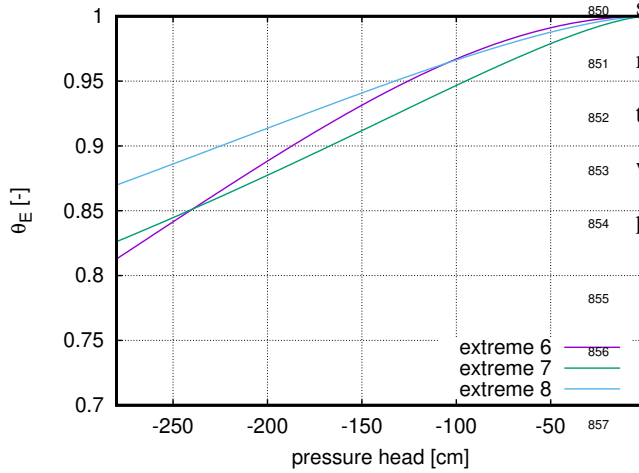


Figure 11: Resulting retention curves obtained from the inverse model.

sarily point to a physically acceptable solution. The most noticeable non-uniqueness was discovered with the saturated water content, since acceptable solutions were identified across extremely broad ranges of this parameter.

- θ_s cannot be reliably obtained by this inverse modeling

- retention curve parameters refer to a relatively similar retention curves at ranges initial condition : boundary condition, see figure 11, unsteady SR experiment seems OK for such identification.

- what else can we say??

5. Acknowledgement

Financial support from ...ADD IGA HERE... is gratefully acknowledged.

References

- Angulo-Jaramillo, R., Vandervaere, J.P., Roulier, S., Thony, J.L., Gaudet, J.P., Vauclin, M., 2000. Field measurement of soil surface hydraulic properties by disc and ring infiltrometers: A review and recent developments. *Soil Tillage Res.* 55, 1–29. doi:10.1016/S0167-1987(00)00098-2.
- Bagarello, V., Prima, S.D., Iovino, M., 2017. Estimating saturated soil hydraulic conductivity by the near steady-state phase of a beerkan infiltration test. *Geoderma* 303, 70 – 77. URL: <http://www.sciencedirect.com/science/article/pii/S001670611730201X>, doi:<https://doi.org/10.1016/j.geoderma.2017.04.030>.

- Bear, J., 1979. Hydraulics of groundwater. McGraw-Hill series in water resources and environmental engineering, McGraw-Hill International Book Co.
- Bellman, R., Åström, K., 1970. On structural identifiability. *Mathematical Biosciences* 7, 329 – 339. URL: <http://www.sciencedirect.com/science/article/pii/002555647090132X>, doi:[https://doi.org/10.1016/0025-5564\(70\)90132-X](https://doi.org/10.1016/0025-5564(70)90132-X).
- Binley, A., Beven, K., 2003. Vadose zone flow model uncertainty as conditioned on geophysical data. *Ground Water* 41, 119–127. URL: <http://dx.doi.org/10.1111/j.1745-6584.2003.tb02576.x>, doi:10.1111/j.1745-6584.2003.tb02576.x.
- Braess, D., 1997. Finite elements: Theory, fast solvers, and applications in solid mechanics. Cambridge University Press.
- Buckingham, E., 1907. Studies on the movement of soil moisture. USDA Bureau of Soils – Bulletin 38.
- Celia, M.A., Bouloutas, E.T., Zarba, R.L., 1990. A general mass-conservative numerical solution for the unsaturated flow equation. *Water Resources Research* 26, 1483–1496. doi:10.1029/WR026i007p01483.
- Cheng, Q., Chen, X., Chen, X., Zhang, Z., Ling, M., 2011. Water infiltration underneath single-ring permeameters and hydraulic conductivity determination. *J. Hydrol.* 398, 135–143. doi:10.1016/j.jhydrol.2010.12.017.
- Christie, I., Griffiths, D.F., Mitchell, A.R., Zienkiewicz, O.C., 1976. Finite element methods for second order differential equations with significant first derivatives. *International Journal for Numerical Methods in Engineering* 10, 1389–1396. URL: <http://dx.doi.org/10.1002/nme.1620100617>, doi:10.1002/nme.1620100617.
- Dusek, J., Dohnal, M., Vogel, T., 2009. Numerical analysis of ponded infiltration experiment under different experimental conditions. *Soil and Water Research* 4, 22–27.
- Fodor, N., Sándor, R., Orfánus, T., Lichner, L., Rajkai, K., 2011. Evaluation method dependency of measured saturated hydraulic conductivity. *Geoderma* 165, 60–68. doi:10.1016/j.geoderma.2011.07.004.
- van Genuchten, M., 1980. Closed-form equation for predicting the hydraulic conductivity of unsaturated soils. *Soil Science Society of America Journal* 44, 892–898. URL: <http://www.scopus.com/inward/record.url?eid=2-s2.0-0019057216&partnerID=40&md5=1a9a45e1c2b571c00ebb9a9f9ebaaf92>.
- van Genuchten, M.T., Simunek, J., Leij, F.J., Sejna, M., 2009. RETC, version 6.02 – code for quantifying the hydraulic functions of unsaturated soils. URL: <http://www.hydrus3d.com>.
- Hrstka, O., Kučerová, A., 2004. Improvements of real coded genetic algorithms based on differential operators preventing premature convergence. *Advances in Engineering Software* 35, 237 – 246. URL: <http://www.sciencedirect.com/science/article/pii/S0965997803001133>, doi:[https://doi.org/10.1016/S0965-9978\(03\)00113-3](https://doi.org/10.1016/S0965-9978(03)00113-3).
- Hwang, S.I., Powers, S.E., 2003. Estimating unique soil hydraulic parameters for sandy media from multi-step outflow experiments. *Advances in Water Resources* 26, 445 – 456. URL: <http://www.sciencedirect.com/science/article/pii/S0309170802001070>, doi:[https://doi.org/10.1016/S0309-1708\(02\)00107-0](https://doi.org/10.1016/S0309-1708(02)00107-0).
- Ibrahimbegović, A., Knopf-Lenoir, C., Kucerova, A., Villon, P., 2004. Optimal design and optimal control of structures undergoing finite rotations and elastic deformations. *International Journal for Numerical Methods in Engineering* 61, 2428–2460.
- Inoue, M., Šimunek, J., Shiozawa, S., Hopmans, J., 2000. Simultaneous estimation of soil hydraulic and solute transport parameters from transient infiltration experiments. *Advances in Water Resources* 23, 677 – 688. URL: <http://www.sciencedirect.com/science/article/pii/S0309170800000117>, doi:[https://doi.org/10.1016/S0309-1708\(00\)00011-7](https://doi.org/10.1016/S0309-1708(00)00011-7).
- Jačka, L., Pavlásek, J., Jindrová, M., Bašta, P., Černý, M., Balvín, A., Pech, P., 2012. Steady infiltration rates estimated for a mountain forest catchment based on the distribution of plant species. *J. For. Sci.* 58, 536–544.
- Jačka, L., Pavlásek, J., Kuráž, V., Pech, P., 2014. A comparison of three measuring methods for estimating the saturated hydraulic conductivity in the shallow subsurface layer of mountain podzols. *Geoderma* 219–220, 82 – 88. doi:10.1016/j.geoderma.2013.12.027.
- Jačka, L., Pavlásek, J., Pech, P., Kuráž, V., 2016. Assessment of evaluation methods using infiltration data measured in heterogeneous mountain soils. *Geoderma* 276, 74 – 83. URL: <http://www.sciencedirect.com/science/article/pii/S0016706116301823>, doi:<http://dx.doi.org/10.1016/j.geoderma.2016.04.023>.
- Kamali, H.R., Zand-Parsa, S., 2016. OPTIMIZATION OF A NEW INVERSE METHOD FOR ESTIMATION OF INDIVIDUAL

- SOIL HYDRAULIC PARAMETERS UNDER FIELD CONDI-
TIONS. Transactions of the ASABE 59, 1257–1266. doi:{10.13031/trans.59.11414}.
- Knobloch, P., 2008. On the choice of the supg parameter at outflow boundary layers. Advances in Computational Mathematics 31, 369. URL: <https://doi.org/10.1007/s10444-008-9075-6>, doi:10.1007/s10444-008-9075-6.
- Kohne, J., Mohanty, B., Simunek, J., 2006. Inverse dual-permeability modeling of preferential water flow in a soil column and implications for field-scale solute transport. Vadose zone journal 5, 59 – 76. doi:<http://dx.doi.org/10.2136/vzj2005.0008>.
- Kool, J., Parker, J., Van Genuchten, M., 1985. Determining soil hydraulic properties from one-step outflow experiments by parameter estimation. i. theory and numerical studies. Soil Science Society of America 49, 1348 – 1354.
- Kowalsky, M., Finsterle, S., Rubin, Y., 2004. Estimating flow parameter distributions using ground-penetrating radar and hydrological measurements during transient flow in the vadose zone. ADVANCES IN WATER RESOURCES 27, 583–599. doi:{10.1016/j.advwatres.2004.03.003}.
- Kucerova, A., 2007. Identification of nonlinear mechanical model parameters based on softcomputing methods. Ph.D. thesis. Ecole Normale Supérieure de Cachan, Laboratoire de Mécanique et Technologie.
- Kuráž, M., Mayer, P., Lepš, M., Trpková, D., 2010. An adaptive time discretization of the classical and the dual porosity model of Richards' equation. Journal of Computational and Applied Mathematics 233, 3167–3177. ISSN: 0377-0427.
- Kuraz, M., Mayer, P., 2008. Drutes – an opensource library for solving coupled nonlinear convection-diffusion-reaction equations. URL: <http://www.drutes.org>.
- Kuraz, M., Mayer, P., 2013. Algorithms for solving darcian flow in structured porous media. Acta Polytechnica 53, 347–358.
- Kuraz, M., Mayer, P., Havlicek, V., Pech, P., 2013a. Domain decomposition adaptivity for the richards equation model. Computing 95, 501–519. URL: <http://dx.doi.org/10.1007/s00607-012-0279-8>, doi:10.1007/s00607-012-0279-8.
- Kuraz, M., Mayer, P., Havlicek, V., Pech, P., Pavlasek, J., 2013b. Dual permeability variably saturated flow and contaminant transport modeling of a nuclear waste repository with capillary barrier protection. Applied Mathematics and Computation 219, 7127 – 7138. doi:<http://dx.doi.org/10.1016/j.amc.2011.08.109>.
- Kuraz, M., Mayer, P., Pech, P., 2014. Solving the nonlinear richards equation model with adaptive domain decomposition. Journal of Computational and Applied Mathematics 270, 2 – 11. URL: <http://www.sciencedirect.com/science/article/pii/S0377042714001502>, doi:<http://dx.doi.org/10.1016/j.cam.2014.03.010>. fourth International Conference on Finite Element Methods in Engineering and Sciences (FEMTEC 2013).
- Kuraz, M., Mayer, P., Pech, P., 2015. Solving the nonlinear and nonstationary richards equation with two-level adaptive domain decomposition (dd-adaptivity). Applied Mathematics and Computation 267, 207 – 222.
- Lassabatère, L., Angulo-Jaramillo, R., Soria Ugalde, J.M., Cuenca, R., Braud, I., Haverkamp, R., 2006. Beerkan estimation of soil transfer parameters through infiltration experiments–best. Soil Science Society of America Journal 70, 521 – 532. doi:<http://dx.doi.org/10.2136/sssaj2005.0026>.
- Leps, M., 2007. Parallel multi-objective identification of material parameters for concrete, in: Proceedings of the Ninth International Conference on the Application of Artificial Intelligence to Civil, Structural and Environmental Engineering, Stirling: Civil-Comp Press Ltd.
- Mous, S., 1993. Identification of the movement of water in unsaturated soils: the problem of identifiability of the model. Journal of Hydrology 143, 153 – 167. URL: <http://www.sciencedirect.com/science/article/pii/0022169493900930>, doi:[https://doi.org/10.1016/0022-1694\(93\)90093-0](https://doi.org/10.1016/0022-1694(93)90093-0). xVI General Assembly of the European Geophysical Society.
- Nakhaei, M., Amiri, V., 2015. ESTIMATING THE UNSATURATED SOIL HYDRAULIC PROPERTIES FROM A REDISTRIBUTION EXPERIMENT: APPLICATION TO SYNTHETIC DATA. JOURNAL OF POROUS MEDIA 18, 717–729.
- Peña-Sancho, C., Ghezzehei, T., Latorre, B., González-Cebollada, C., Moret-Fernández, D., 2017. Upward infiltration–evaporation method to estimate soil hydraulic properties. Hydrological Sciences Journal 62, 1683–1693. URL: <https://doi.org/10.1080/02626667.2017.1343476>, doi:10.1080/02626667.2017.1343476, arXiv:<https://doi.org/10.1080/02626667.2017.1343476>.
- Ramos, T., Goncalves, M., Martins, J., van Genuchten, M., Pires,

- F., 2006. Estimation of soil hydraulic properties from numerical inversion of tension disk infiltrometer data. *VADOSE ZONE JOURNAL* 5, 684–696. doi:10.2136/vzj2005.0076.
- Reynolds, W.D., 2008a. Saturated hydraulic properties: Ring infiltrometer, in: Carter M.R., Gregorich, E.G. [Eds.], *Soil Sampling and Methods of Analysis*, 2nd ed. CRC Press Taylor & Francis, Boca Raton, USA, pp. 1043–1056.
- Reynolds, W.D., 2008b. Saturated hydraulic properties: Well permeameter, in: Carter M.R., Gregorich, E.G. [Eds.], *Soil Sampling and Methods of Analysis*, 2nd ed. CRC Press Taylor & Francis, Boca Raton, USA, pp. 1025–1042.
- Rezaei, M., Seuntjens, P., Shahidi, R., Joris, I., Boënné, W., Al-Barri, B., Cornelis, W., 2016. The relevance of in situ and laboratory characterization of sandy soil hydraulic properties for soil water simulations. *Journal of Hydrology* 534, 251 – 265. URL: <http://www.sciencedirect.com/science/article/pii/S0022169416000044>, doi:<http://dx.doi.org/10.1016/j.jhydrol.2015.12.062>.
- Richards, L.A., 1931. Capillary conduction of liquids through porous mediums. *Journal of Applied Physics* 1, 318–333. doi:10.1063/1.1745010.
- Roos, H., G., Stynes, M., Tobiska, L., 1996. *Numerical Methods for Singularly Perturbed Differential Equations, Convection-Diffusion and Flow Problems*. Springer-Verlag Berlin Heidelberg.
- Rypl, D., 2004. T3D Mesh Generator. Department of Mechanics, CTU in Prague, Czech Republic. Prague, Czech Republic. URL: <http://mech.fsv.cvut.cz/~dr/t3d.html>.
- Saltelli, A., Chan, K., Scott, E., 2000. *Sensitivity Analysis*. Wiley series in probability analysis, John Wiley & Sons.
- Schaap, M.G., Leij, F.J., van Genuchten, M.T., 2001. rosetta: a computer program for estimating soil hydraulic parameters with hierarchical pedotransfer functions. *J. Hydrol.* 251, 163 – 176. doi:[http://dx.doi.org/10.1016/S0022-1694\(01\)00466-8](http://dx.doi.org/10.1016/S0022-1694(01)00466-8).
- Scharnagl, B., Vrugt, J.A., Vereecken, H., Herbst, M., 2011. Inverse modelling of in situ soil water dynamics: investigating the effect of different prior distributions of the soil hydraulic parameters. *Hydrology and Earth System Sciences* 15, 3043–3059. URL: <http://www.hydrol-earth-syst-sci.net/15/3043/2011/>, doi:10.5194/hess-15-3043-2011.
- Schwartz, R., Evett, S., 2002. Estimating hydraulic properties of a fine-textured soil using a disc infiltrometer. *SOIL SCIENCE SOCIETY OF AMERICA JOURNAL* 66, 1409–1423.
- Simunek, J., van Genuchten, M., T., Gribb, M., Hopmans, J.W., 1998. Parameter estimation of unsaturated soil hydraulic properties from transient flow processes1. *Soil Tillage Res.* 47, 27 – 36. doi:[http://dx.doi.org/10.1016/S0167-1987\(98\)00069-5](http://dx.doi.org/10.1016/S0167-1987(98)00069-5).
- Simunek, J., Wendroth, O., van Genuchten, M., 1999. Estimating unsaturated soil hydraulic properties from laboratory tension disc infiltrometer experiments. *WATER RESOURCES RESEARCH* 35, 2965–2979. doi:{10.1029/1999WR900179}.
- Swartzendruber, D., 1987. A Quasi-Solution of Richards Equation for the Downward Infiltration of Water into Soil. *Water Resour. Res.* 23, 809–817. doi:10.1029/WR023i005p00809.
- Ventrella, D., Losavio, N., Vonella, A., Leij, F., 2005. Estimating hydraulic conductivity of a fine-textured soil using tension infiltrometry. *Geoderma* 124, 267 – 277. doi:<http://dx.doi.org/10.1016/j.geoderma.2004.05.005>.
- Verbist, K., Cornelis, W.M., Gabriels, D., Alaerts, K., Soto, G., 2009. Using an inverse modelling approach to evaluate the water retention in a simple water harvesting technique. *HYDROLOGY AND EARTH SYSTEM SCIENCES* 13, 1979–1992.
- Vitingerova, Z., 2010. *Evolutionary Algorithms for Multi-Objective Parameter Estimation*. Ph.D. thesis. CTU in Prague, Fac. of Civil Eng.
- Xu, X., Lewis, C., Liu, W., Albertson, J., Kiely, G., 2012. Analysis of single-ring infiltrometer data for soil hydraulic properties estimation: Comparison of best and wu methods. *Agricultural Water Management* 107, 34 – 41. URL: <http://www.sciencedirect.com/science/article/pii/S0378377412000200>, doi:<https://doi.org/10.1016/j.agwat.2012.01.004>.
- Younes, A., Mara, T., Fahs, M., Grunberger, O., Ackerer, P., 2017. Hydraulic and transport parameter assessment using column infiltration experiments. *Hydrology and Earth System Sciences* 21, 2263–2275. URL: <https://www.hydrol-earth-syst-sci.net/21/2263/2017/>, doi:10.5194/hess-21-2263-2017.
- Zou, Z.Y., Young, M., Li, Z., Wierenga, P., 2001. Estimation of depth averaged unsaturated soil hydraulic properties from infiltration experiments. *Journal of Hydrology* 242, 26 – 42. URL: <http://www.sciencedirect.com/science/article/pii/S0022169400003851>, doi:[http://dx.doi.org/10.1016/S0022-1694\(00\)00385-1](http://dx.doi.org/10.1016/S0022-1694(00)00385-1).

Appendix A. Solutions after the first identification run with $r_f = 0$ and $r_f = 1$.

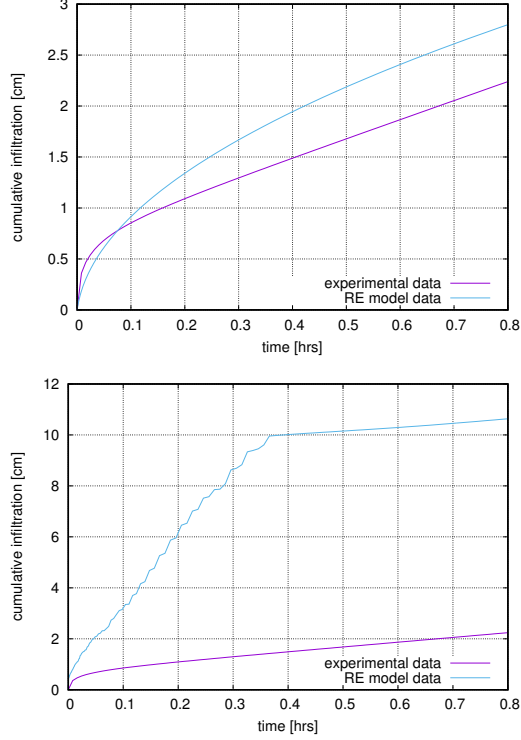


Figure A.12: Refinement level $r_f = 0$: Local extreme 1 , Right: Local extreme 2.

Appendix B. Scatter plots for objective functions, $r_f = 0, 1$

Scatter plots of the objective functions for the local extreme 6 are depicted in figures Appendix B – Appendix B.

Scatter plots of the objective functions for the local extreme 7 are depicted in figures Appendix B – Appendix B.

Scatter plots of the objective functions for the local extreme 8 are depicted in figures Appendix B – Appendix B.

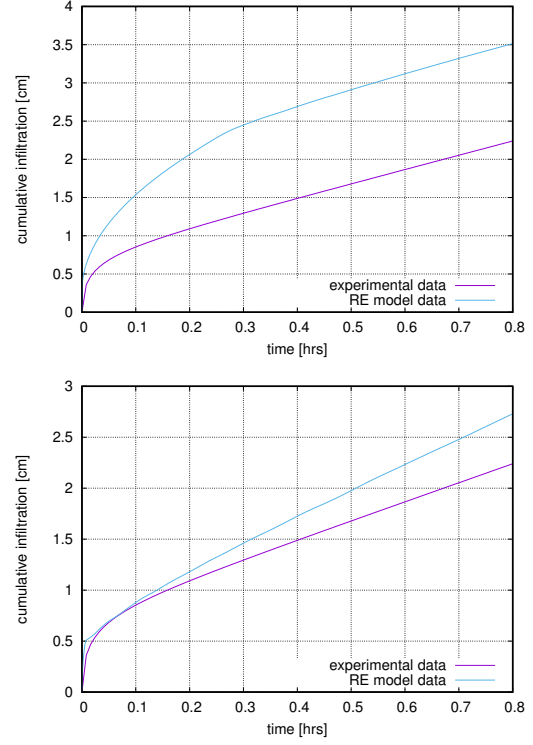


Figure A.13: Refinement level $r_f = 0$: Local extreme 3 , Right: Local extreme 4.

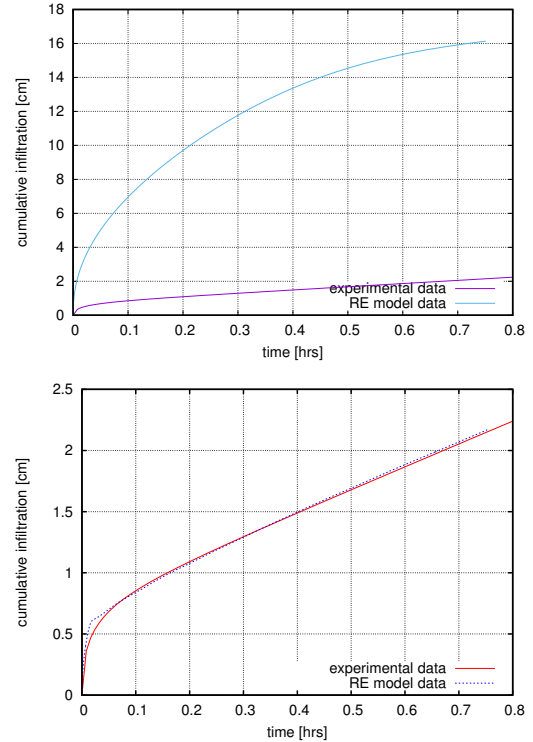


Figure A.14: Refinement level $r_f = 0$: Local extreme 5 , Right: Local extreme 6.

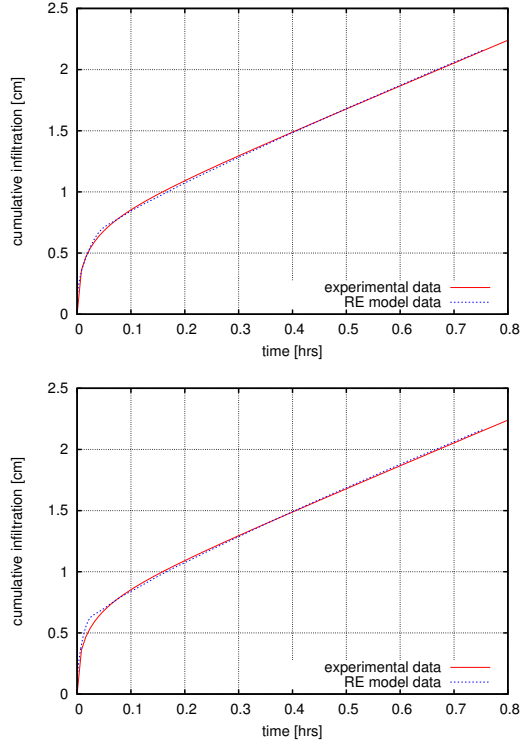


Figure A.15: Refinement level $r_f = 0$: Local extreme 7, Right: Local extreme 8.

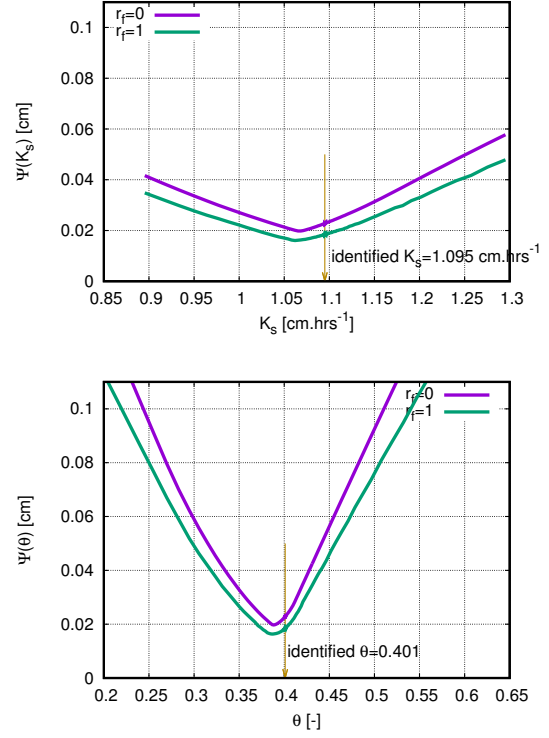


Figure B.17: Scatter plots for $r_f = 0, 1$ for extreme 6 for parameters K_s and θ_s .

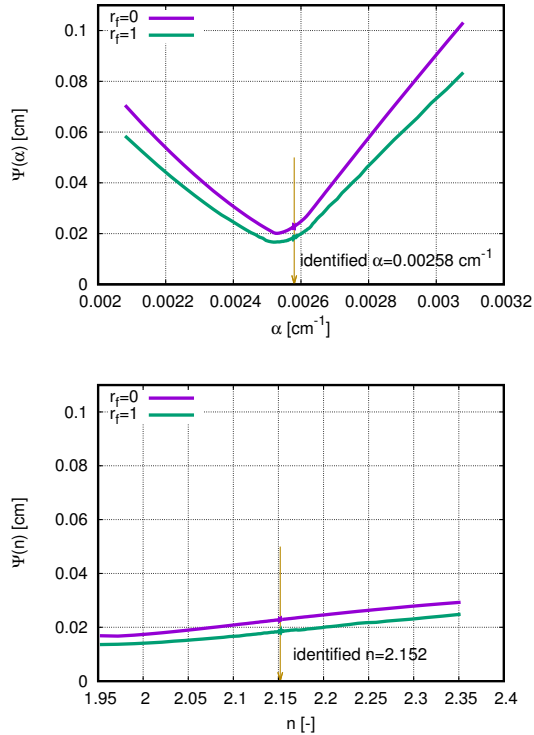


Figure B.16: Scatter plots for $r_f = 0, 1$ for extreme 6 for parameters α and n .

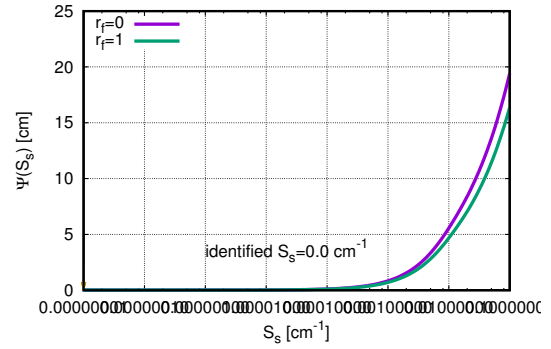


Figure B.18: Scatter plots for $r_f = 0, 1$ for extreme 6 for parameter S_s

1149 Appendix C. New solutions for $r_f = 1$

1150 The updated solutions for the local extremes 7 and
1151 8 are depicted in figures Appendix C and Appendix
1152 C.

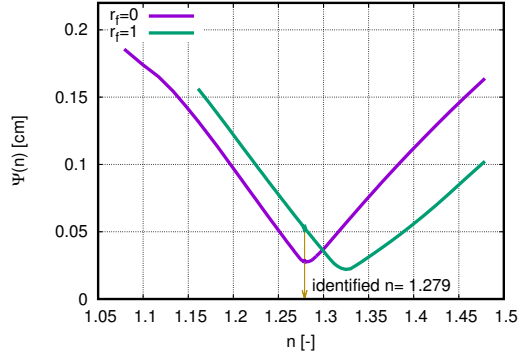
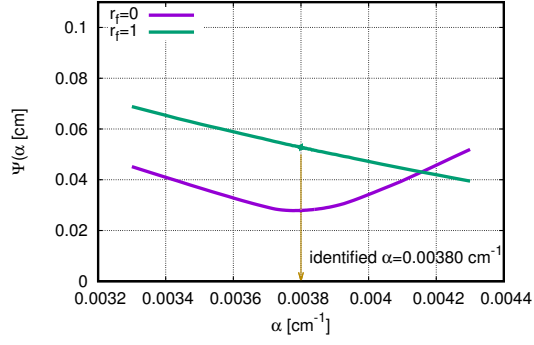


Figure B.19: Scatter plots for $r_f = 0, 1$ for extreme 7 for parameters α and n .

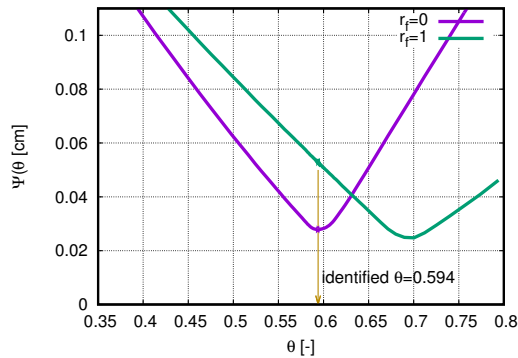
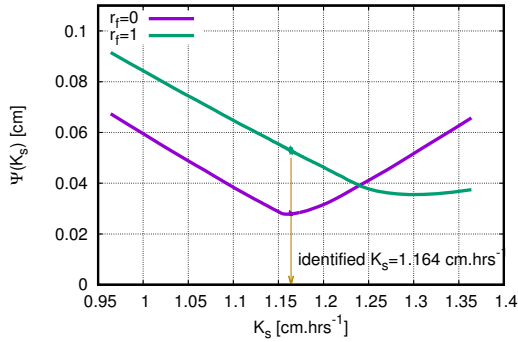


Figure B.20: Scatter plots for $r_f = 0, 1$ for extreme 7 for parameters K_s and θ_s .

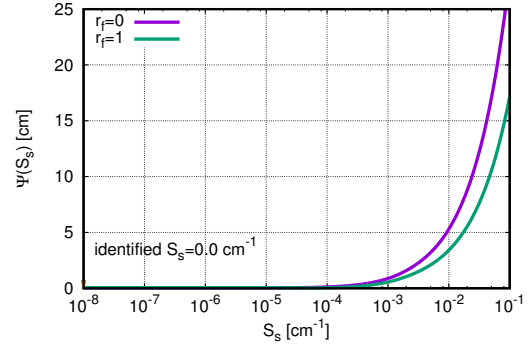


Figure B.21: Scatter plots for $r_f = 0, 1$ for extreme 7 for parameter S_s .

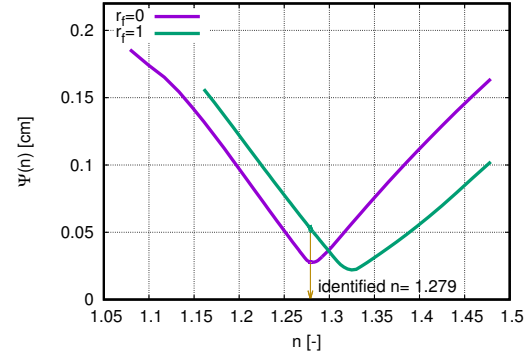
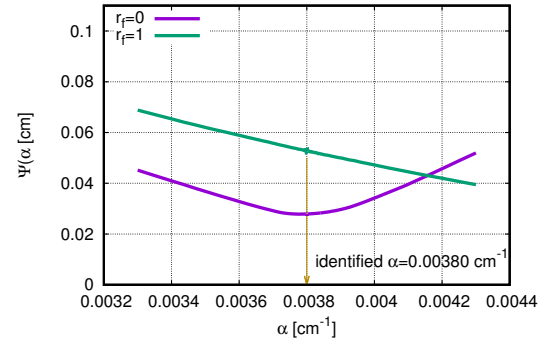


Figure B.22: Scatter plots for $r_f = 0, 1$ for extreme 8 for parameters α and n .

Appendix D. Scatter plots for objective functions, $r_f = 1, 2$

Scatter plots of the objective functions for the updated local extreme 7 for $r_f = 1, 2$ is depicted in figures Appendix D - Appendix D.

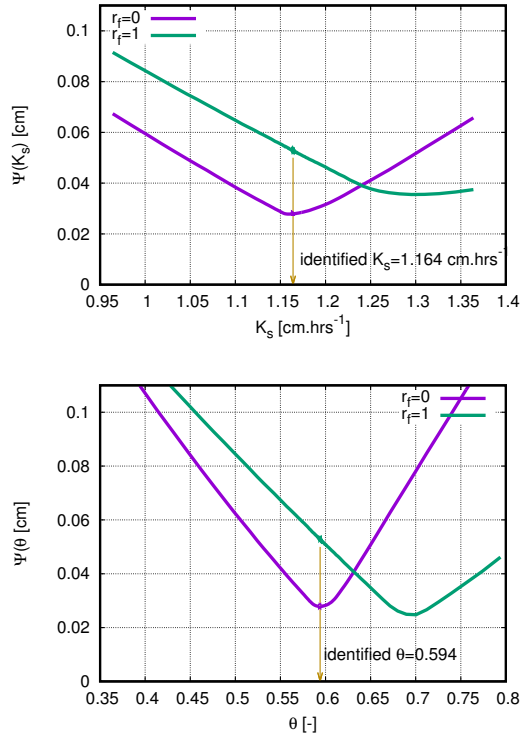


Figure B.23: Scatter plots for $r_f = 0, 1$ for extreme 8 for parameters K_s and θ_s .

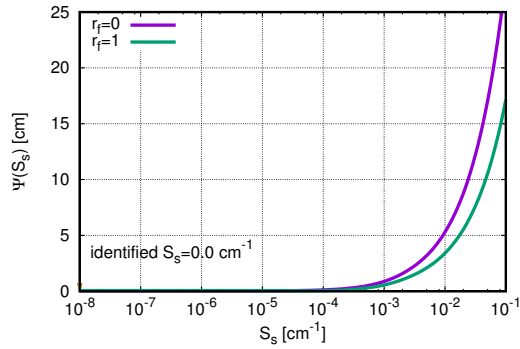


Figure B.24: Scatter plots for $r_f = 0, 1$ for extreme 8 for parameter S_s .

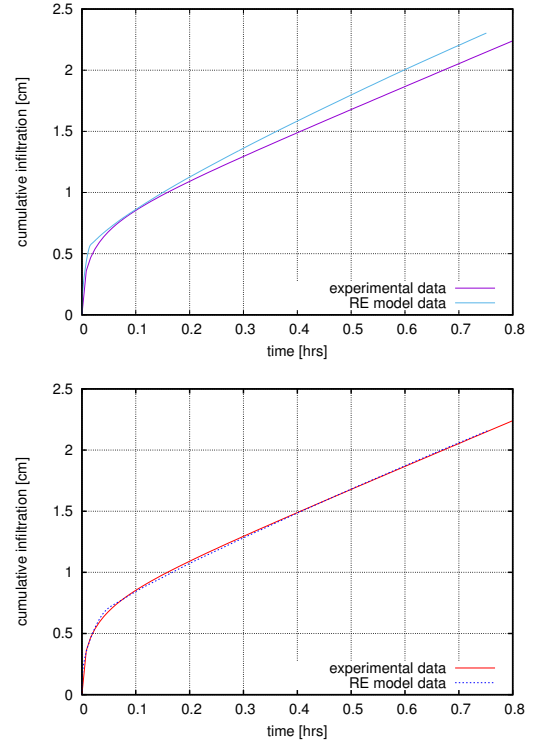


Figure C.25: Left: Local extreme 7 infiltration curve for the original parameter set obtained at $r_f = 0$ and solved on model with discretization $r_f = 1$, right: solution for the updated parameter set in vicinity of the extreme 7.

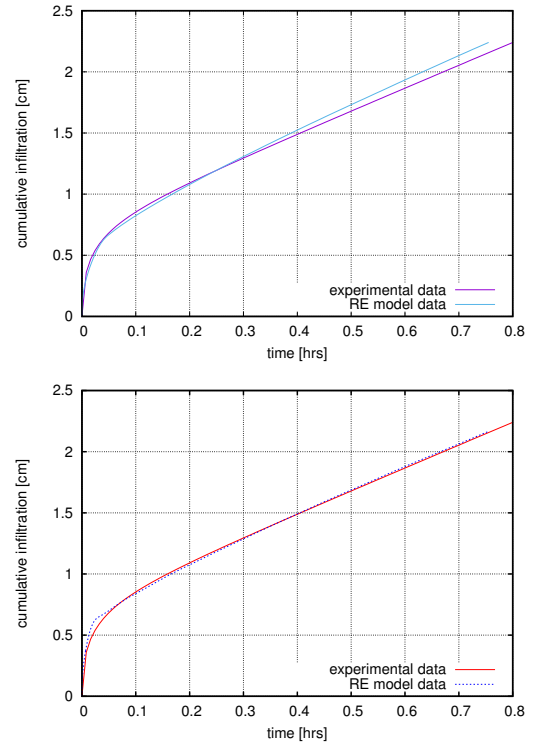


Figure C.26: Left: Local extreme 8 infiltration curve for the original parameter set obtained at $r_f = 0$ and solved on model with discretization $r_f = 1$, right: solution for the updated parameter set in vicinity of the extreme 7.

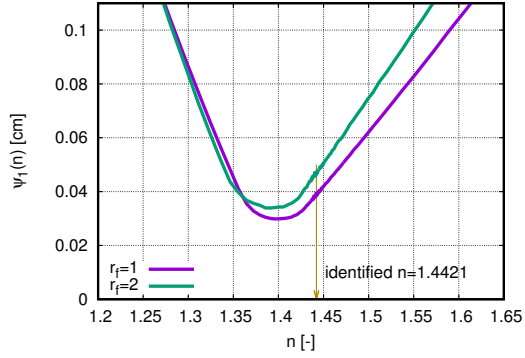
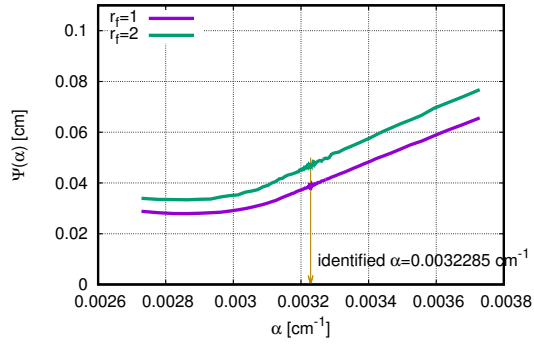


Figure D.27: Scatter plots for $r_f = 1, 2$ for extreme 7 for parameters α and n .

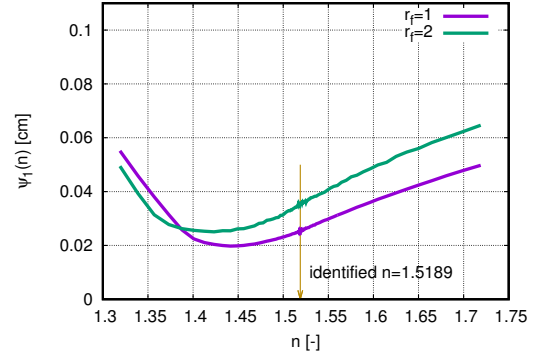
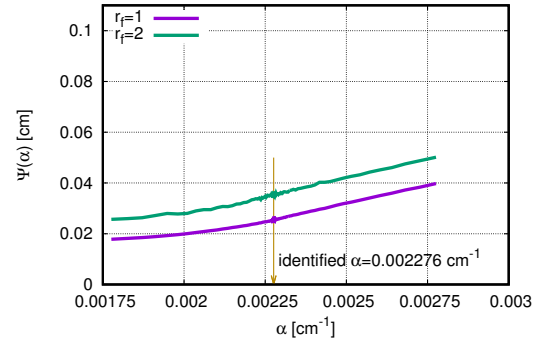


Figure D.29: Scatter plots for $r_f = 1, 2$ for extreme 8 for parameters α and n .

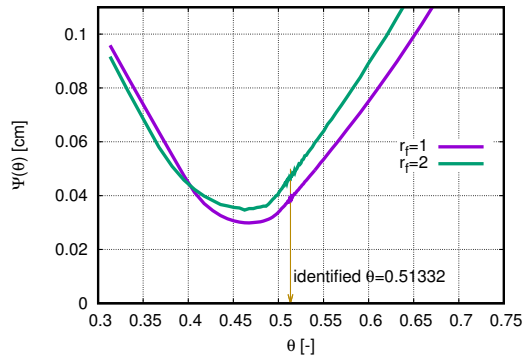
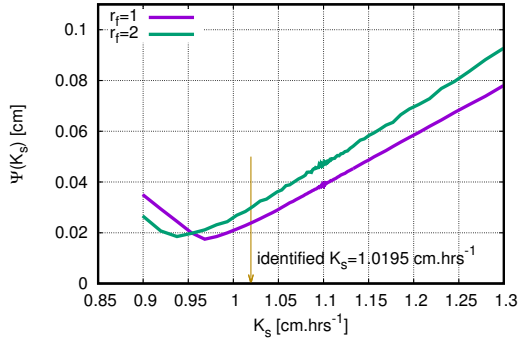


Figure D.28: Scatter plots for $r_f = 1, 2$ for extreme 7 for parameters K_s and θ_s .

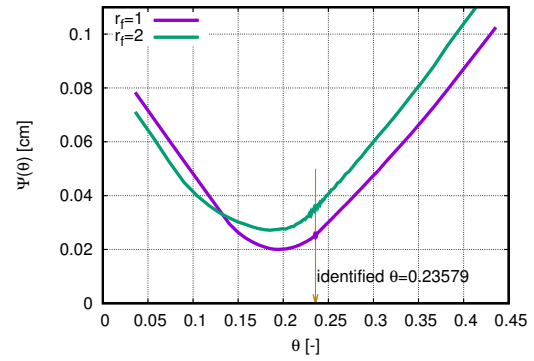
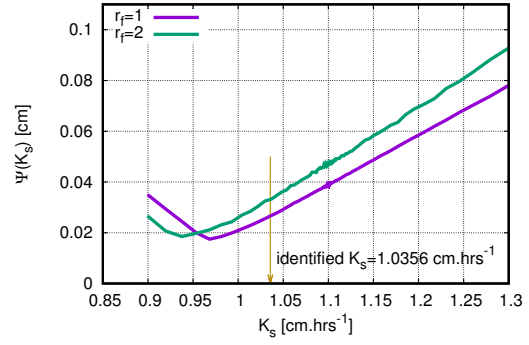


Figure D.30: Scatter plots for $r_f = 1, 2$ for extreme 8 for parameters K_s and θ_s .